Breakup of the projectile in ^{16}O-induced reactions on ^{27}Al, ^{58}Ni, and ^{197}Au targets around 100 MeV/nucleon

A. Badalà, R. Barbera, A. Palmeri, and G. S. Pappalardo
Istituto Nazionale di Fisica Nucleare, Sezione di Catania, Corso Italia 57, 95129 Catania, Italy

F. Riggi
Istituto Nazionale di Fisica Nucleare, Sezione di Catania, Corso Italia 57, 95129 Catania, Italy
and Dipartimento di Fisica dell'Università di Catania, Corso Italia 57, 95129 Catania, Italy
(Received 26 February 1993)

The spatial correlation among the four He ions coming from the disassembly of the ^{16}O projectile on ^{27}Al, ^{58}Ni, and ^{197}Au targets has been studied at 94 MeV/nucleon. Charged particles have been detected by a multielement array of plastic scintillators covering the angular domain between 3° and 150°. Standard relativistic kinematics has been used to reconstruct the excitation energy of the primary projectilelike nucleus (E^*_{PLN}). Mean values of this quantity are found independent of the target mass and the comparison with existing similar data taken at lower bombarding energies shows a saturation of E^*_{PLN} around 3 MeV/nucleon. An event-by-event analysis has been performed in order to study the distributions of some global variables such as coplanarity, sphericity, and relative angle, helpful in the understanding of the topological characteristics of the process and in the evaluation of its time scale. Experimental data have also been compared with the results of Monte Carlo simulations based on different reaction mechanisms and it is possible to conclude that sequential emission of the fragments is preferred.

PACS number(s): 25.70.Mn

I. INTRODUCTION

Two very important goals in the study of heavy-ion reactions at intermediate energies are the understanding of the space-time evolution of the interacting system [1–42] and the solution of the related problem concerning the existence of a limit for the excitation energy that a nucleus can sustain before its breaking [43–56]. In the last few years, the first of these aims has been pursued through the analysis of both angular correlations between light charged particles at small (intensity interferometry technique) [1–7] and large (coincidence azimuthal angular distributions study) [8–22] relative momenta, and suitable global variable distributions [24–42] related to the event shape in momentum space [24–35] or to the topological distribution of the particles in configuration space [7–22,34–42]. The study of the two-particle correlation functions at small relative momenta with the assumption of spherical sources of negligible lifetime [7] shows that the correlation distance which can be directly compared with the source size is independent of the target mass. This result is in agreement with the conclusions of Refs. [12,22] in which the azimuthal angular distribution of projectilelike particles have been measured in coincidence with light charged particles. Moreover, if one takes into account the temporal contribution to the correlation distance [2], it is possible to calculate emission times of the order of several tens of fm/c in accordance with those calculated by a dynamical model in Ref. [22]. Strong final-state interactions (due to the short times involved) [22] and momentum conservation limitations [8–23] as well as collective motions [15,16,36–42] also play an important role as one can see from the trend of the asymmetries in the azimuthal angular distributions in the reaction plane and out of the reaction plane as a function of the target mass and incident energy. Mean field effects such as angular momentum ones are also present at lower energies (especially for heavy targets) [9–11,23], but they disappear at higher ones [17,23].

The question about the excitation energy limitation for a nucleus in heavy-ion collisions has been investigated with various projectiles such as ^{40}Ar [44–47], ^{84}Kr [48], and ^{208}Pb [49] on different heavy targets from ^{103}Rh to ^{238}U in the incident energy range between 27 and 77 MeV/nucleon. In these experiments multiplicities of neutrons [45,47–49] and light charged particles [44–46] associated with central collisions have been measured in coincidence with projectilelike fragments [44,48,49], targetlike ones [47–49], and fission fragments [46,48,49]. Unfortunately, no compelling evidence for the existence of a limit of the excitation energy is yet observable in experimental data relative to heavy systems and selecting small impact parameters. So, recently, some attention has been turned to the study of projectile breakup [31,34,35,50–56] in peripheral collisions induced by light nuclei such as ^{12}C [50,54], ^{16}O [31,34,35,50,51,54–56], ^{20}Ne [52], ^{28}Si [53], and ^{32}S [51] on different targets spanning the whole stable mass range at bombarding energies from 12.5 to 94 MeV/nucleon. The projectile disassembly channels involving charged particles have been observed in those events where the total detected charge was equal to the projectile one. The excitation energy of the primary projectilelike nuclei was reconstructed from the measured kinetic energies of the individual fragments in the event center of mass. The authors of Refs. [52,53], and those of Refs. [50,51,54–56], who have analyzed the

systems $^{28}Si+^{28}Si$ and $^{16}O+^{197}Au$, respectively, conclude that there is a possible saturation of the projectile excitation energy around 3 MeV/nucleon with an increase of the bombarding energy, independent of the particular decay channel. In Ref. [56] it is also shown that this value is independent of the target mass.

Two goals in the understanding of the breakup mechanism are to explain the spatial correlations among the emitted fragments and to determine the process time scale, i.e., whether the splitting of the highly excited projectile takes place instantaneously or following a sequence of binary, fissionlike steps. At low energies [31–35,50–54] (up to about 30 MeV/nucleon), the data are well reproduced by theoretical calculations based on a sequential binary fission emission [28,57,58], while at higher energy no exhaustive calculation exists, although there is some evidence in the system $^{40}Ar+^{51}V$ [32,33] at 65 and 85 MeV/nucleon that could be described in a multifragmentation picture. The spatial distribution of the projectile breakup products has been previously analyzed in Ref. [54], for two-body decay channels in the reaction $^{16}O+^{197}Au$ at 32.5 MeV/nucleon, and in Ref. [35], where a study was performed concerning the projectile angular momentum effect and the target proximity effects such as final-state interactions, shadowing, etc., for the reaction $^{159}Tb(^{16}O,4He)$ at 25 MeV/nucleon. No work exists for such light projectiles at higher incident energies.

In this paper we report on an experiment in which the 4 He breakup channel of the ^{16}O projectile has been studied at 94 MeV/nucleon bombarding energy in reactions induced on different targets spanning a wide range of nuclear masses. The paper is organized as follows. Section II is devoted to a description of the experimental setup and selection criteria on treated data. In Sec. III a general review of the results of data analysis is shown. Section IV concerns an event shape study conducted through the analysis of some global variable distributions in both configuration and momentum space. Experimental data are also compared with the results of different theoretical calculations based on sequential and prompt emission of the particles in order to evaluate the process time scale. Summary and conclusions are given in Sec. V.

II. EXPERIMENT AND DATA SELECTION CRITERIA

The experiment discussed in the present paper was performed at GANIL. A ^{16}O beam at 94 MeV/nucleon was pulsed with a repetition rate of 13.5 MHz on ^{27}Al, ^{58}Ni, and ^{197}Au targets. The full width at half maximum (FWHM) of the beam pulse was 1 ns. The target thicknesses used were 6.76 mg/cm^2 for the Al, 8.9 mg/cm^2 for the Ni, and 19.3 mg/cm^2 for the Au.

A. Detection system

The overall detection apparatus is sketched in Fig. 1. Light charged particles have been detected by two large-area multidetectors, which were able to identify the charge Z from hydrogen to oxygen by a standard ΔE-TOF (time of flight) technique. The TOF start was given

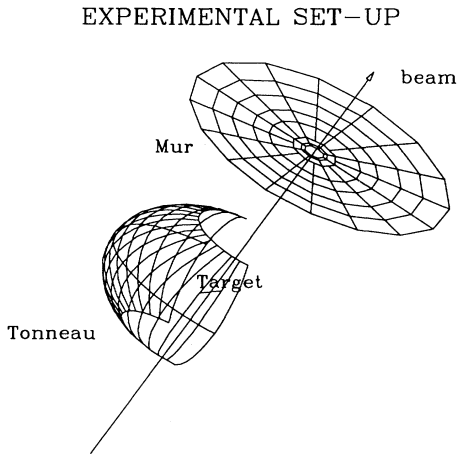

FIG. 1. Global view of the experimental setup.

by the rf signal delivered by the machine. The multidetectors used in this experiment were the *Mur* (plastic wall) [59] and one half of the *Tonneau* (plastic barrel) [60], installed in the *Nautilus* vacuum chamber at the GANIL facility.

The Mur consists of an array of 96 NE102 plastic scintillators, 2 mm thick, arranged in seven concentric rings located at angles of 4°, 6°, 8.5°, 12°, 16.5°, 21.5°, and 27° with respect to the beam, covering the whole azimuthal domain. All the counters were placed 210 cm from the target position, subtending a total solid angle of 0.85 sr.

Larger angles, from 30° to 150°, were covered by the Tonneau, which consists of 36 staves of NE102 plastic scintillators, 2 mm thick. The Tonneau covered only half of the azimuthal angular range, between 90° and 270°, in steps of 10° (see Fig. 1). The detectors of the Tonneau were placed 80 cm from the target position, subtending a

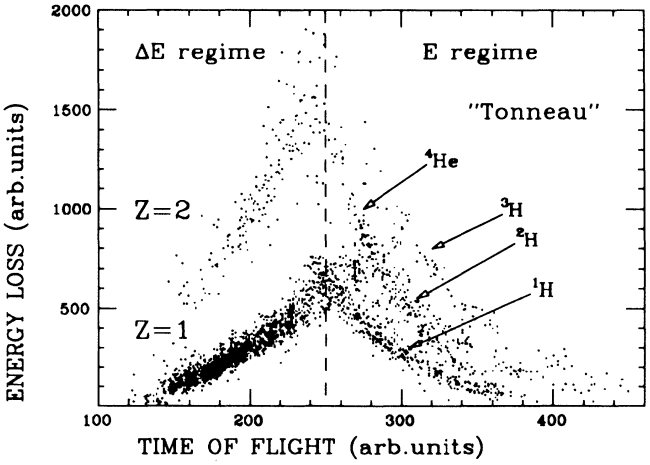

FIG. 2. Typical energy loss versus time of flight plot (ΔE-TOF) of an element of the Tonneau. To the left of the dashed line (which corresponds to a stopping range of ~15 MeV/nucleon for protons and helium ions), the particles cross the detector (ΔE regime). On the right side the particles are stopped within the detector (E regime).

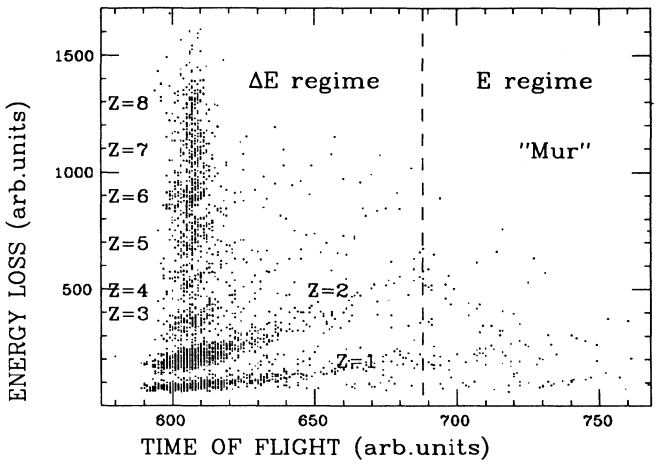

FIG. 3. As in Fig. 2 for a plastic scintillator of the first ring of the Mur.

total solid angle of 5.44 sr. The light output of each scintillator was monitored at both ends by two photomultipliers. This allowed a determination of the crossing point of the charged particle through the transit duration time difference $(t_1 - t_2)$ of the light signals as measured at the two extremities. The uncertainty in the angle with respect to the beam was about $\pm 6°$. Aluminum foil, 200 μm thick, was placed in front of each plastic counter of both multidetectors to absorb soft radiation.

A very clean separation of the different charges was obtained only for particles crossing the scintillators (ΔE regime), while those stopped in the detectors (E regime) could not be easily identified. A velocity threshold of about 5 cm/ns (corresponding to an energy threshold of about 15 MeV/nucleon for H and He ions) was thus imposed due to the thickness of the detectors and of the aluminum foil absorber.

In Fig. 2 a typical ΔE-TOF scatter plot for an element of the Tonneau is shown. $Z=1$ particles are clearly separated from $Z=2$ particles only in the ΔE regime. Figure 3 shows a ΔE-TOF scatter plot relative to an element of the first ring of the Mur. All particles are moving essentially with beam velocity, and they all fall in the ΔE region. All charges from $Z=1$ up to $Z=8$ are visible.

B. Selection of projectile breakup events

Although the detection system allowed for the identification of all charges from $Z=1$ up to the projectile, in this work we restricted our analysis to $Z=2$ fragments. In accordance with Refs. [31,34,35,50,54–56,58], in the off-line analysis we selected only those events where the total collected charge was equal to the charge of the projectile. This condition, coupled with the velocity threshold due to particle identification, eliminated nearly any contribution of low-energy particles coming by an excited targetlike nucleus [54].

The mass-symmetric channel 4 He has the least ambiguity with respect to the isotopic makeup of the final nuclei, and all $Z=2$ fragments are treated as ^{4}He [31,34,35]. Moreover, because of spatial symmetry reasons, we took into account only those He ions firing the detectors of the Mur. For the particles measured by the Tonneau, only the total multiplicity information was considered in the present work.

Typical velocity spectra of He ions detected with the ^{197}Au target are shown in Fig. 4 for those events containing only four $Z=2$ particles. In each plot right and left arrows indicate the projectile velocity and the compound nucleus velocity, respectively. The phenomenology of this kind of reaction between heavy ions at intermediate energies generally shows the fragmentation of projectile and the formation of a participant zone. These two components are visible in the velocity spectra. The first one is

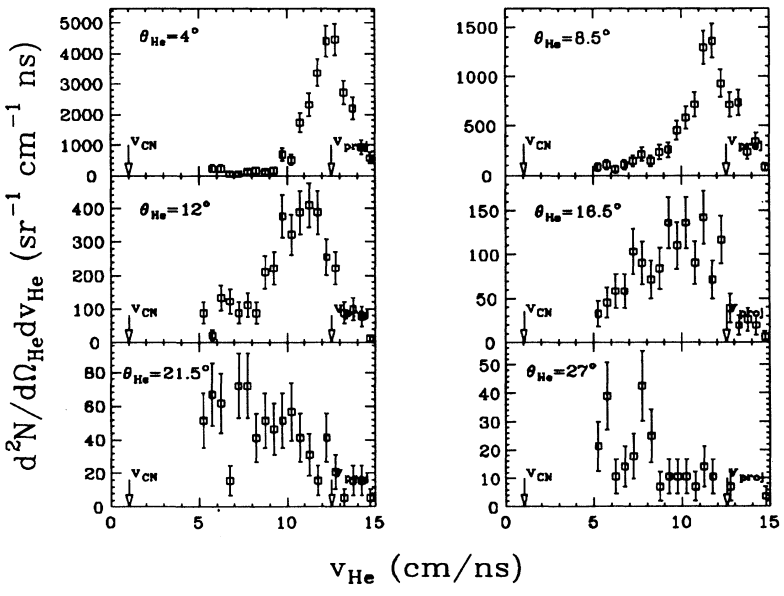

FIG. 4. Velocity distributions of the He ions detected in the ^{16}O+^{197}Au reaction at 94 MeV/nucleon. Only those events containing four $Z=2$ particles are plotted. In each plot right and left arrows indicate the projectile velocity and the compound nucleus velocity, respectively.

centered close to the projectile velocity and appears primarily at forward angles. The second one is centered around half of the beam velocity and is attributed to a more relaxed source [22,61]. The latter is present at all angles and becomes the main contribution when the angle with respect to the beam increases beyond 20°. This seems quite reasonable since the grazing angles for the reactions induced by ^{16}O at 94 MeV/nucleon on ^{27}Al, ^{58}Ni, and ^{197}Au are 0.7°, 1.4°, and 3°, respectively.

In the present paper we restricted the analysis to the events with only four particles with $Z=2$, all detected in the angular range between 3° and 20° (the first five rings of the Mur; see Fig. 1) with a velocity larger than 8 cm/ns. These severe conditions reasonably select those events resulting from the breakup of the primary projectilelike nucleus (PLN). Figure 5 shows the total measured parallel momentum (divided by the projectile momentum) distributions for the three different targets for those events where only He ions were detected in the Mur. The peaks correspond to different multiplicities of $Z=2$ particles. As one can see the 4-He events are reasonably *well measured* [30]; i.e., the projectile momentum is almost completely reconstructed. By means of standard relativistic kinematics [62], we have also reconstructed the velocity of the center of mass of the fragments detected in these events. The peripheral nature of the reaction was verified by observing the distribution of this quantity for each of the three targets, shown in Fig. 6. The PLN velocities are peaked very close to the beam velocity, and moreover, no evidence of a target-mass dependence is observed.

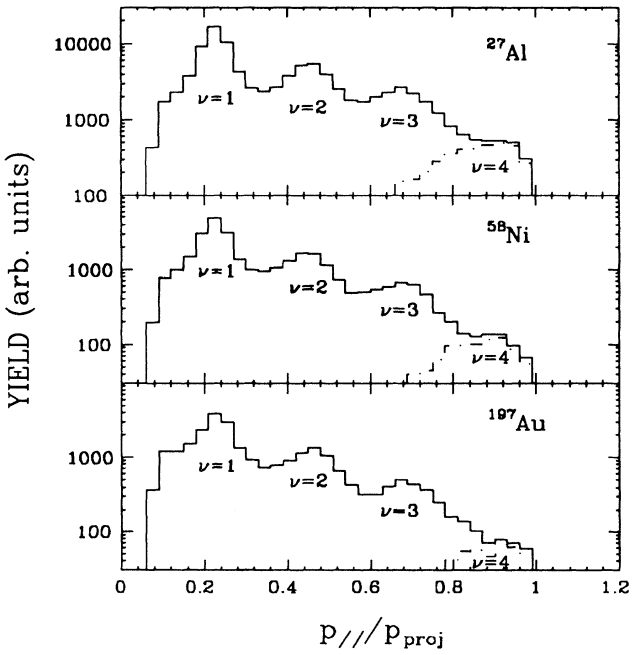

FIG. 5. Total parallel momentum (divided by the projectile momentum) distributions for the three different targets relative to those events where only He ions were detected in the Mur. The different peaks correspond to different multiplicities of $Z=2$ particles.

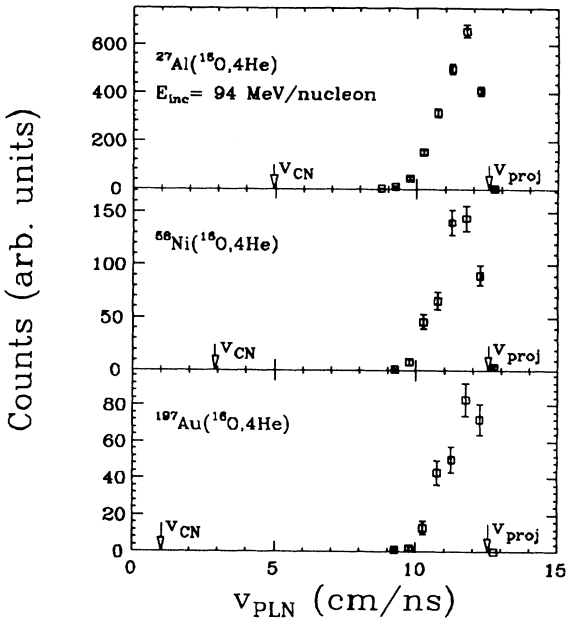

FIG. 6. Velocity distributions of the 4-He center of mass for the ^{27}Al, ^{58}Ni, and ^{197}Au targets. In each histogram the arrows indicate the projectile velocity (v_{proj}) and the compound nucleus velocity (v_{CN}).

C. Efficiency

A Monte Carlo simulation of the breakup process via a binary sequential decay has been performed in order to evaluate the detector efficiency as a function of the detection angle and excitation energy (see next section) of the projectilelike nucleus. The calculation takes into account the complete geometry of the experimental setup and contains the measured angular distribution of the primary fragment and its velocity distribution. The effects of the efficiency correlation on the experimental data are in agreement with the results of Ref. [55], obtained with a very similar multidetector, and will be discussed in more detail in the next sections.

III. RESULTS

A. Excitation energy spectra

The excitation energy of the primary projectilelike nucleus can be calculated [54] as the sum over the relative kinetic energies K_{He} of all fragments detected in an event in the rest frame of the PLN, shifted by the Q value of the 4-He breakup channel:

$$E^*_{PLN} = \sum_{\nu=1}^{4} K_{He_\nu} + Q_{^{16}O\rightarrow 4He} \ . \quad (1)$$

In Fig. 7 the excitation energy distributions for the different targets are shown. The spectral shapes are quite similar. They exhibit a maximum centered at around 30–35 MeV and an exponential tail which has the same slope for the three targets. The arrows in Fig. 7 indicate the Q value for the 4-He channel. Only the falloff to Q of

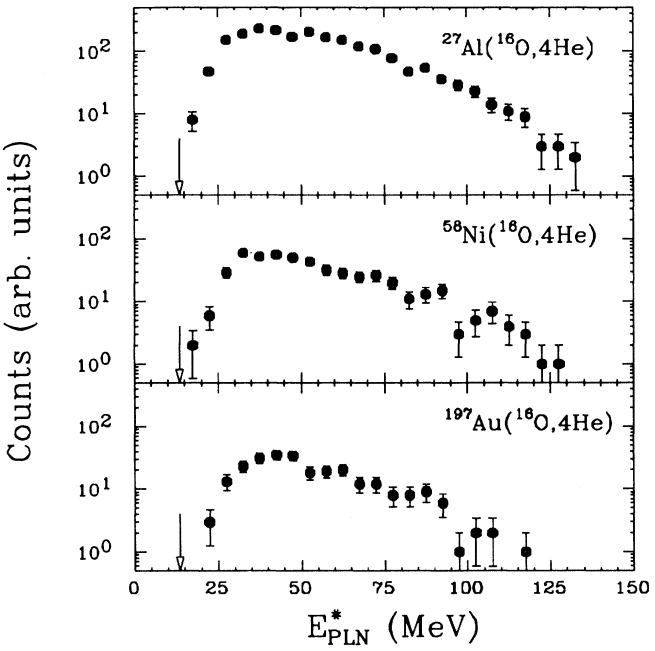

FIG. 7. Experimental excitation energy distributions of the primary projectilelike nucleus for the three different targets at 94 MeV/nucleon. The arrows indicate the limit due to the mass conservation ($Q_{^{16}O\rightarrow 4He}$).

the excitation energy distributions is slightly different for the various targets. It is sharper for the Al target than for the heavier ones. This could be explained as an effect of the repulsive interaction of the fragments with the target's Coulomb potential. Figure 8 shows the PLN excitation energy distribution for the Au target compared to those obtained for the same target at lower bombarding energies [55]. The spectra have been normalized to the same number of counts. The shape of the spectrum taken at 94 MeV/nucleon is very similar to that of the spectrum taken at 70 MeV/nucleon both in slope and location of the maximum. In Table I (third and fourth columns), the mean values of the extracted PLN excitation energies E^*_{PLN} and the values of the slope p of the excitation energy spectra are reported as a function of the target mass and bombarding energy. The errors listed are statistical. The same value is found for the three targets, indicating that the breakup process, for the observed channel, has to be related mainly to the internal structure of the projectile. E^*_{PLN} values show a slight increase with the incident energy going from 30 MeV at 32.5 MeV/nucleon [55] to 53 MeV at 70 MeV/nucleon [55]. The mean value of 54±2 MeV at 94 MeV/nucleon is equal, within the error bars, to that observed at 70 MeV/nucleon, revealing a saturation of the excitation energy which can be stored in such a projectile, for the observed disassembly channel. This value has been obtained by imposing the previously mentioned conditions on the detection angle ($\theta \leq 20°$) and particle velocity ($v > 8$ cm/ns). Slightly varying these conditions, we find a value of 53±2 MeV, taking into account all particles with $\theta \leq 14.5°$ (the first four rings of the Mur) and $v > 7$ cm/ns, and a value of 58±2 MeV, taking into account all particles with $\theta \leq 20°$ and $v > 7$ cm/ns, which are still compatible with the value extracted at 70 MeV/nucleon. The extreme value of 58±2 MeV found with the low-velocity threshold is probably too high due to the fact that He ions from the more relaxed source [22,61] are included in the analysis. The penultimate column of Table I contains the values p_{corr}, which are the slopes of the excitation energy spectra taking into account the detector efficiency correction. The trend of the experimental data both with target mass and bombarding energy is confirmed also for these efficiency-corrected data.

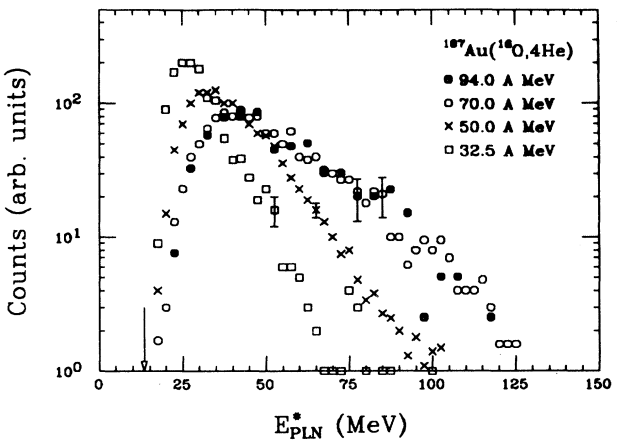

FIG. 8. Experimental excitation energy distributions of the primary projectilelike nucleus for the breakup process ^{16}O→4He in the reaction ^{16}O+^{197}Au at different bombarding energies. The data have been normalized to the same number of counts. The arrow indicates the limit due to the mass conservation ($Q_{^{16}O\rightarrow 4He}$). The data at 32.5, 50, and 70 MeV/nucleon come from Ref. [54].

B. Excitation energy sharing

Important hints for understanding the reaction mechanism can be obtained through the study of the excitation energy sharing between the projectile and the target [54,55]. In fact, this energy sharing must lie between two extremes: (i) the equal temperature limit (ETL), when the interaction time is long enough for the target and projectile to reach thermal equilibrium and the total excitation energy is shared according to the ratio of their masses, and (ii) the equal energy sharing limit (EES), where the excitation energy is shared equally, on the average, between projectile and target as a consequence of fast nucleon-nucleon exchanges.

In order to study this excitation energy sharing, we calculate, on an event-by-event basis, the target excitation energy (which is called available energy E^*_{avl}). This quantity can be evaluated by imposing total energy conservation:

$$E^*_{avl} = E_{beam} - K_{PLN} - K_{tgt} - E^*_{PLN} , \quad (2)$$

where K_{PLN} is the kinetic energy of the primary projectilelike nucleus, obtained from v_{PLN}, and K_{tgt} is the kinet-

TABLE I. Third and fourth columns report the mean values of the extracted PLN excitation energies E^*_{PLN} and the values of the slope p of the excitation energy spectra as a function of the target mass (first column) and bombarding energy (second column). The fifth column contains the values p_{corr} of the slopes of the excitation energy spectra taking into account the detector efficiency correction. The last column contains the values of the ratio $R = E^*_{avl}/E^*_{PLN}$ between the most probable excitation energies of the target and projectile for the system $^{16}O+^{197}Au$ at different bombarding energies. All errors are statistical. The data at 32.5, 50, and 70 MeV/nucleon come from Ref. [54].

Target	E_{beam}	E^*_{PLN}	p	p_{corr}	R
^{197}Au	32.5A MeV	30 MeV	8.0 MeV	10.9 MeV	2.6
^{197}Au	50.0A MeV	40 MeV	12.0 MeV	17.3 MeV	3.3
^{197}Au	70.0A MeV	53 MeV	18.0 MeV	22.7 MeV	3.7
^{197}Au	94.0A MeV	54±2 MeV	21.0±4.0 MeV	22.0±2.0 MeV	2.9±1.7
^{58}Ni	94.0A MeV	54±1 MeV	21.0±4.0 MeV	22.7±3.0 MeV	
^{27}Al	94.0A MeV	54±1 MeV	19.0±2.0 MeV	22.1±1.2 MeV	

ic energy of the targetlike nucleus, evaluated from the momentum conservation equation $\mathbf{P}_{beam}=\mathbf{P}_{tgt}+\mathbf{P}_{PLN}$. The distributions of the available energy for all three targets are plotted in Fig. 9. These spectra show very broad maxima around 100–200 MeV and an exponential decrease up to more than 600 MeV. However, these surprisingly high tails have relatively large errors and could be explained by the combined effects of the residual contamination of the particles coming from the relaxed source and the finite energy resolution due to the temporal structure of the beam pulse. In fact, this is justified by observing that PLN velocity distributions of Fig. 6 are slightly skewed to the left (see Table II) and that for a velocity of about 8–9 cm/ns the energy resolution is ~10%.

The last column of Table I contains the values of the ratio $R = E^*_{avl}/E^*_{PLN}$ between the most probable (peak position [54,55]) excitation energies of the target and projectile for the system $^{16}O+^{197}Au$ at different bombarding energies. The large asymmetry of this system helps discriminate between the two different possibilities: ETL ($R=12$) or EES ($R=1$). The value $R=2.9\pm1.7$ found at 94 MeV/nucleon is in agreement with those extracted at lower incident energies [54,55] and suggests quite rapid energy sharing between projectile and target, very far from a thermally equilibrated system picture.

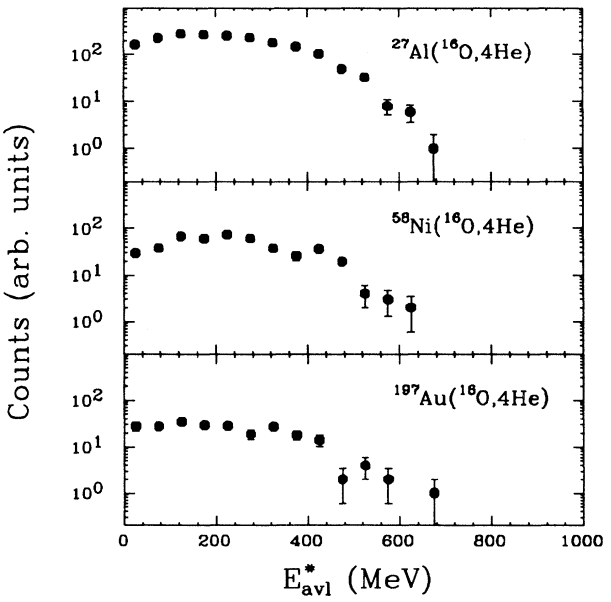

FIG. 9. Experimental distributions of the available energy (see text) for the three different targets at 94 MeV/nucleon.

C. PLN angular distributions

In Fig. 10 experimental PLN angular distributions for the different targets are reported. Open symbols refer to raw data, while solid ones refer to efficiency-corrected data. All the spectra show an exponential decrease with practically the same slope. In the case of the Au target, the points at low angles differ from the common behavior, displaying a change in the slope both for raw and corrected data. This might be explained by an orbiting effect, due to the large mass of the heaviest target, which would deflect the trajectories of the fragments inside the forward hole of the Mur. The effect is visible only for this target because of the large grazing angle of the reaction $^{16}O+^{197}Au$ at 94 MeV/nucleon (about 3°), which almost coincides with the minimum detection angle of the experimental setup.

D. Fragment spatial distribution in the PLN frame

The analysis of the projectilelike nucleus excitation energy spectra gave no evidence of target mass dependence as was seen both in the mean values of E^*_{PLN} and the slope parameters p. In order to study more closely PLN angular momentum effects and possible target influences through final-state interactions and/or shadowings, the

TABLE II. Statistical moments of the PLN velocity distributions for the three targets.

Target	Mean	Std. dev.	Skewness	Kurtosis
^{27}Al	11.41 cm/ns	0.66 cm/ns	−0.67	3.08
^{58}Ni	11.40 cm/ns	0.64 cm/ns	−0.48	2.71
^{197}Au	11.53 cm/ns	0.63 cm/ns	−0.67	2.86

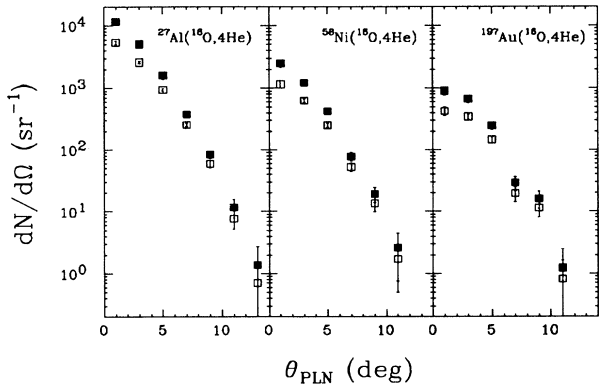

FIG. 10. Experimental PLN angular distributions for the various studied reactions. Open symbols refer to raw data, while solid ones refer to efficiency-corrected data.

spatial distribution of 4-He breakup fragments has been analyzed in the PLN rest frame on an event-by-event basis. The chosen system of reference $\{O'X'Y'Z'\}$ is shown in Fig. 11. The Z' axis is oriented in the same direction of the PLN velocity vector. The X' axis is oriented along the impact parameter direction. The Y' axis is perpendicular to the X'-Z' plane, and it is chosen in the same direction of the angular momentum. The angles η and χ are defined by the He ion velocity direction in the PLN rest frame with Y' and Z' axes, respectively. The angle ψ is the azimuthal angle in the plane X'-Y'.

The η angular distributions for the three different targets are plotted in Fig. 12. In order to visualize possible differences in shape of these distributions as a function of the target, the data of ^{58}Ni and ^{197}Au have been normalized to those of ^{27}Al. The solid curves shown in Fig. 12 correspond to an isotropic emission of the fragments in the PLN system of reference. As one can easily see, no angular momentum effect is visible at this incident energy for any of the targets, unlike Ref. [35] where a value of $I=5\hbar$ for the oxygen projectile reproduces the experimental data more closely than $I=0\hbar$, in the reaction ^{159}Tb(^{16}O,4He) at 25 MeV/nucleon.

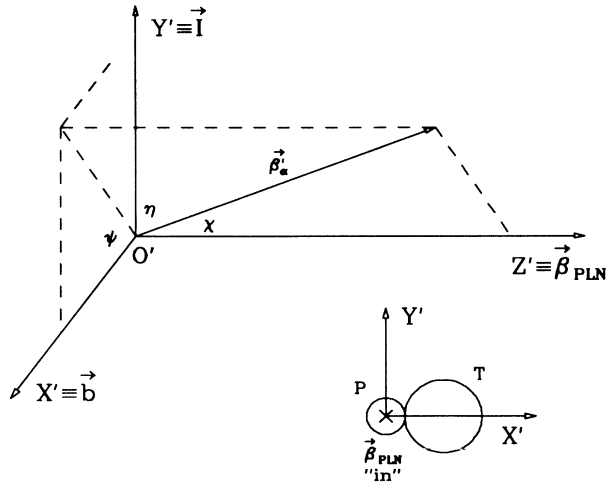

FIG. 11. Reference system $\{O'X'Y'Z'\}$ in the PLN rest frame. The Z' axis is oriented in the same direction of the PLN velocity vector. The X' axis is oriented along the impact parameter direction. The Y' axis is perpendicular to the X'-Z' plane, and it is chosen in the same direction of the angular momentum. The angles η and χ are defined by the He ion velocity direction in the PLN rest frame with Y' and Z' axes, respectively. The angle ψ is the azimuthal angle in the plane X'-Y'.

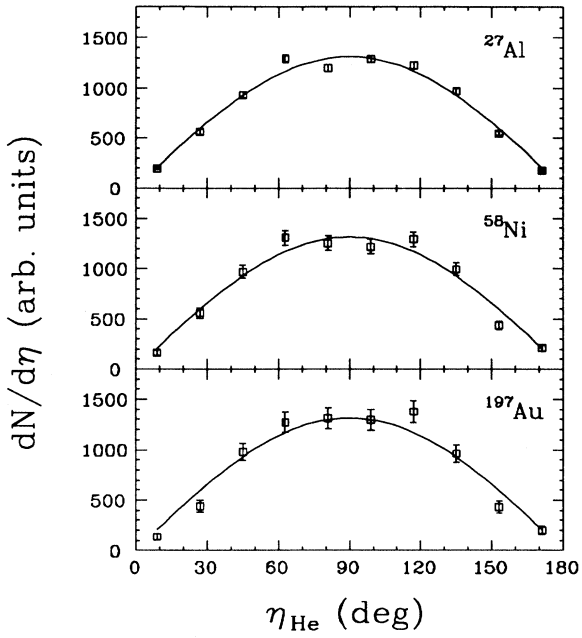

FIG. 12. Distributions of the angle η for the three different targets. In order to visualize possible differences in shape of these distributions as a function of the target, the data of ^{58}Ni and ^{197}Au have been normalized to those of ^{27}Al. The solid curves are relative to an isotropic emission of the fragments in the PLN reference frame.

Figures 13–15 show the χ angular distributions for the various targets. The upper and lower parts of these figures are for those He ions which have an X' component of their velocity lower and larger than zero, respectively. The term "in plane" means that only fragments with $-30°<\psi<30°$ have been considered. Similarly, the solid curves plotted in Figs. 13–15 correspond to an isotropic emission of the fragments in the two hemispheres (see inset in Fig. 11) of the PLN rest frame. The particles going into the left hemisphere are preferentially scattered at angles larger than those expected by an isotropic emission due to the repulsive action of the Coulomb field of the target. The particles going into the right hemisphere are subject to two effects: (i) at low and high χ angles, the number of detected He ions is higher than that expected from an isotropic emission due to the attractive action of the nuclear field of the target, and (ii) around $\chi=90°$, the number of emitted fragments is lower than that relative to an isotropic emission; this could be explained by a shadowing effect due to the presence of

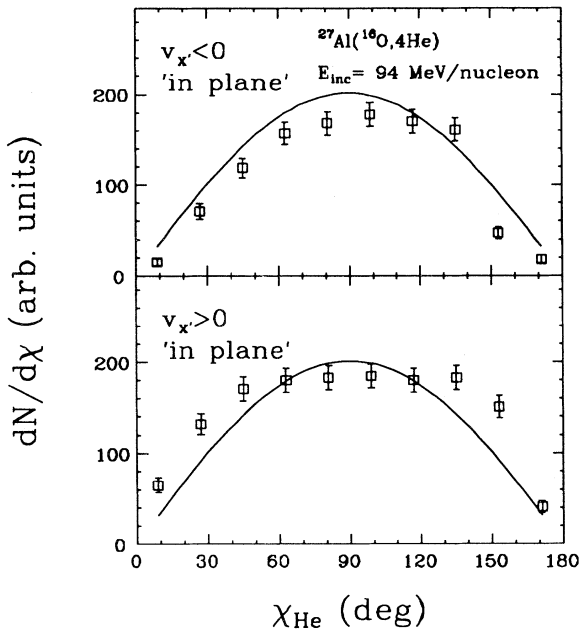

FIG. 13. Distribution of the angle χ for the ^{27}Al target. The upper and lower parts of this figure are relative to those He ions which have a X' component of their velocity lower and larger than zero, respectively. The term "in plane" means that only fragments with $-30° < \psi < 30°$ have been considered. The solid curves are relative to an isotropic emission of the fragments in the PLN rest frame.

the target in this direction (see Fig. 11). These effects are clearly visible in the case of the Al target. For the heavier targets they should be more evident, but this is not so apparent due to the low statistics.

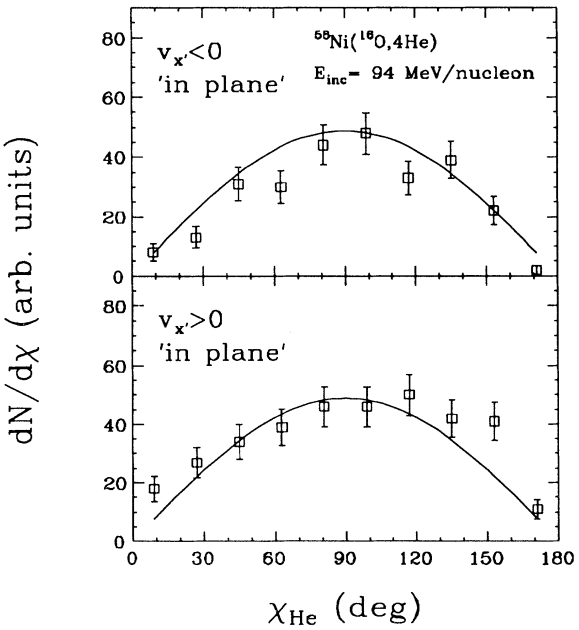

FIG. 14. As in Fig. 13 for the ^{58}Ni target.

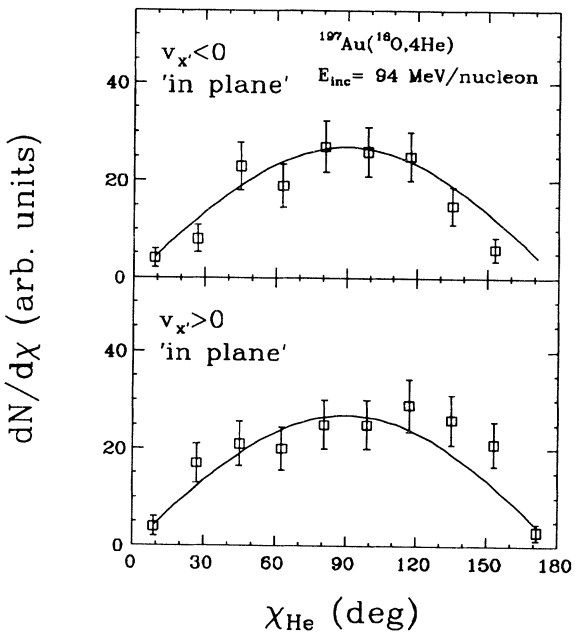

FIG. 15. As in Fig. 13 for the ^{197}Au target.

E. Charged particle multiplicity associated with breakup events

The study of particle multiplicities can be a qualitative tool to demonstrate the peripheral character of the projectile breakup reactions. In Fig. 16 the multiplicity distributions of charged particles in the Tonneau are shown for the three different systems when a 4-He event, verify-

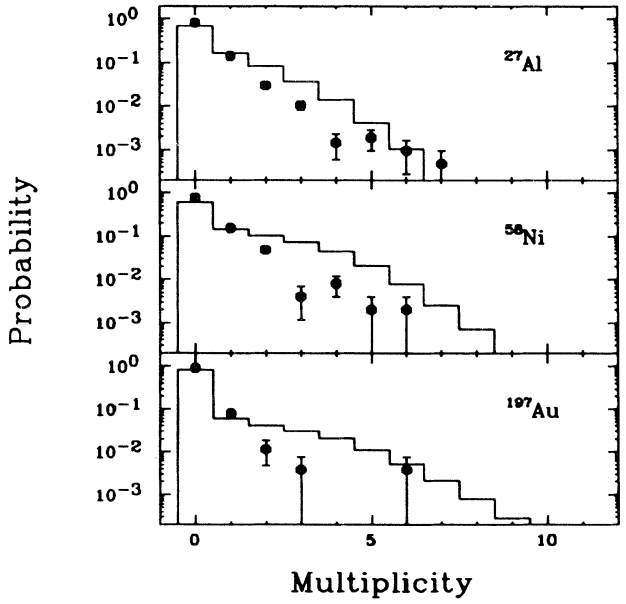

FIG. 16. Normalized multiplicity distributions of charged particles firing the Tonneau when a 4-He event is registered by the Mur (points) and for the minimum bias (histogram).

ing the previously mentioned detection angle and velocity conditions, is registered by the Mur (points). The histograms indicate the minimum bias multiplicity distributions. As one can see, in almost all breakup events no charged particles are detected at angles larger than 30°. In fact, the probability to have zero particles in the Tonneau, $P(\nu=0)$, is $\sim 80\%$ with the Al and Ni targets and more than 90% with the Au target. Moreover, the slopes of the 4-He multiplicity distributions are steeper than the minimum bias multiplicity distributions for all targets.

In Fig. 17 are plotted the mean charged particle multiplicities observed in the Tonneau (corresponding to breakup event detected by the Mur) as a function of the available energy in the target, for all three reactions. For the two lighter targets, these multiplicities show an increase with increasing target excitation energy as expected for evaporation [35]. Unfortunately, in the Au case the low statistics do not allow us to draw any conclusions.

F. Total cross section of the breakup process

In order to give a quantitative estimate of the cross section of the breakup process, we calculated the ratio P between the number of breakup events, taking into account the efficiency correction and the number of events where at least two charged particles hit the overall detection setup without charge identification requirement and, therefore, velocity threshold requirement (a minimum bias condition). This quantity is reported in Table III for the three targets. Within a simple geometrical framework, it is possible to calculate a breakup cross section of about 10 mb for all targets.

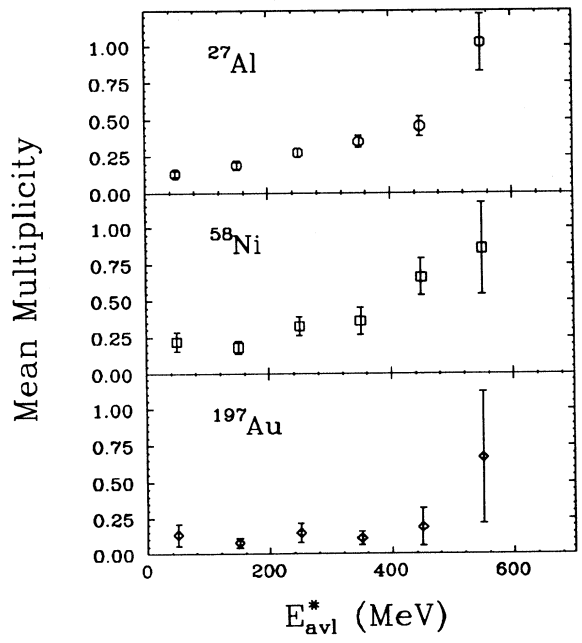

FIG. 17. Mean charged particle multiplicities observed in the Tonneau, corresponding to breakup event detected by the Mur, as a function of the available energy (see text) for the various studied reactions.

TABLE III. First row contains the total number of recorded events, for the three studied reactions, where at least two charged particles hit the detector setup without charge identification requirement and, therefore, velocity threshold. The second row contains the number of breakup events selected by means of the cuts in velocity and detection angle of He ions discussed in the text. In the third row the number of breakup events taking into account the detector efficiency correction is reported. The last row contains the probability P of the breakup process. The errors are statistical.

Events	^{27}Al	^{58}Ni	^{197}Au
$N_{\nu\geq 2}$	534 091	196 494	149 591
N_{breakup}	2100	498	264
$N^{\text{corr}}_{\text{breakup}}$	3958	936	487
P	$7.4(1)\times 10^{-3}$	$4.8(2)\times 10^{-3}$	$3.3(1)\times 10^{-3}$

IV. GLOBAL VARIABLE ANALYSIS

The experimental data have been submitted to an event-by-event analysis performed to extract some global variable distributions that could describe the entire fragmenting system [27,28] and investigate the process time scale [31–35].

A. Sphericity and coplanarity

From the velocity vectors of all emitted fragments in the PLN rest frame, one can construct the kinetic flow tensor [27]

$$T_{ij}=\frac{1}{4}\sum_{\nu=1}^{4} v_i^{(\nu)} v_j^{(\nu)} \tag{3}$$

and calculate its eigenvectors and eigenvalues. The eigenvectors $\mathbf{e}_1$, $\mathbf{e}_2$, and $\mathbf{e}_3$ associated with the eigenvalues $\lambda_1\geq\lambda_2\geq\lambda_3\geq 0$ determine an ellipsoid in velocity space whose shape can be expressed in terms of sphericity (S) and coplanarity (C) variables defined as [27,28]

$$S=\frac{3}{2}\frac{\lambda_2+\lambda_3}{\lambda_1+\lambda_2+\lambda_3} \tag{4}$$

and

$$C=\frac{\sqrt{3}}{2}\frac{\lambda_2-\lambda_3}{\lambda_1+\lambda_2+\lambda_3}\ . \tag{5}$$

The specific values $(S,C)=(0,0)$, $(\frac{3}{4},\sqrt{3}/4)$, and (1,0) characterize, respectively, pure pencil-like, disklike, and spherical events.

Event distributions in the coplanarity-sphericity (C-S) plane for the three different targets are shown in Fig. 18. Average values $\langle S\rangle$ and $\langle C\rangle$ are reported in Table IV for all targets. The errors are the statistical ones. For the ^{197}Au target the values are also compared with those extracted at 32.5 MeV/nucleon [31]. The low values at 32.5 MeV/nucleon have been taken from Refs. [31,34] as an indication of a sequential decay process. A comparison of the C-S distributions with the theoretical calculations of some semiclassical dynamical models [28,57,58] indeed confirms this interpretation. The higher values of

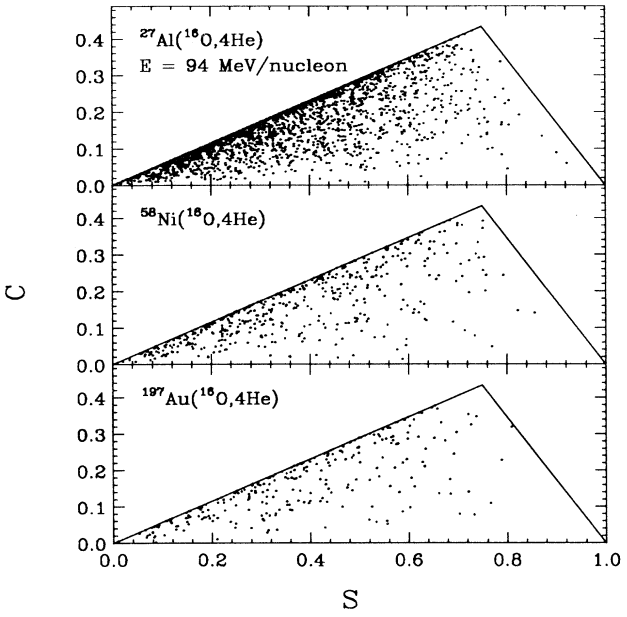

FIG. 18. Experimental distributions in the coplanarity-sphericity plane of the 4-He breakup events for the three different targets at 94 MeV/nucleon.

$\langle S \rangle$ and $\langle C \rangle$ found at 94 MeV/nucleon could be attributed to a more prompt decay process, but we have to be aware that our analysis of data in terms of coplanarity and sphericity is relative to events with only four particles, and this low multiplicity can introduce large fluctuations in the coplanarity and sphericity mean values [26,63]. Thus, in this context, it is very hard to conclude that this is evidence for a prompt breakup process (multifragmentation).

To go beyond the information contained in the experimental average values of C and S, we have compared the data with theoretically generated distributions, following the prescriptions reported in Ref. [64]. The sequential emission of fragments (SEQ) has been simulated by a random distribution of the relative angles and momenta of the four He ions in phase space with only the constraint of momentum conservation. This apparently oversimplified approach is justified by the independence of which statistical formalism is effectively used in the simulation, as has been shown in Ref. [35]. The time intervals between the different binary fission steps are assumed to be so long that no interaction among the emitted fragments is taken into account, whereas for a given sequential-fission event its multifragmentation (MF) partner is generated by repositioning all the sequential-fission fragments randomly within a small spherical volume (the freeze-out volume) and then following their trajectories as they disassemble under the influence of their mutual Coulomb repulsion [28]. The four α particles are placed in a random nonoverlapping configuration with their centers confined within a sphere whose volume is twice that of the nuclear volume of the ^{16}O. This freeze-out configuration is then propagated dynamically in time, under the action of the repulsive Coulomb field, by a Runge-Kutta numerical integration of the equations of motion, until the fragments have attained their asymptotic velocities. Both SEQ and MF calculations contain the initial experimental excitation energy distribution of the PLN as well as their velocity and angular distributions, and take into account the geometric limitations of the experimental setup and the cuts on velocity and detection angle imposed in the data analysis. Figure 19 shows the C-S results of SEQ and MF calculations for 500 ^{197}Au(^{16}O,4He) breakup events at 32.5 MeV/nucleon incident energy. The comparison with the experimental data (see Fig. 3 of Ref. [31] and Fig. 4 of Ref. [34]) confirms the sequential character of the disassembly process at this bombarding energy. A good agreement is also achieved with calculations based on different theoretical models described in Refs. [28,57,58], validating our previous hypotheses. The C-S plots for SEQ and MF breakup are compared with the experimental plot at 94 MeV/nucleon in Fig. 20. The data are for the ^{27}Al target, and the number of simulated events is equal to the number of experimental events (see Table III). The data are reproduced by the sequential emission, and no compelling evidence for a multifragmentation of the projectile

TABLE IV. Mean values of the sphericity and coplanarity for the three different targets. The data relative to the ^{197}Au(^{16}O,4He) events are compared with those extracted at 32.5 MeV/nucleon [31]. The errors are statistical.

Target	E_{beam}	$\langle S \rangle$	$\langle C \rangle$
^{27}Al	94.0A MeV	0.366±0.004	0.159±0.002
^{58}Ni	94.0A MeV	0.365±0.008	0.154±0.004
^{197}Au	94.0A MeV	0.378±0.011	0.160±0.006
^{197}Au	32.5A MeV	0.191±0.004	0.101±0.002

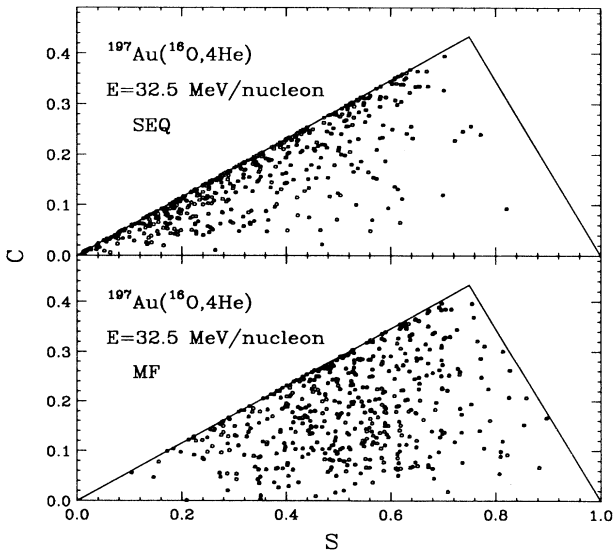

FIG. 19. Simulated sphericity-coplanarity distributions for SEQ and MF calculations described in the text relative to the reaction ^{16}O+^{197}Au→4He at 32.5 MeV/nucleon.

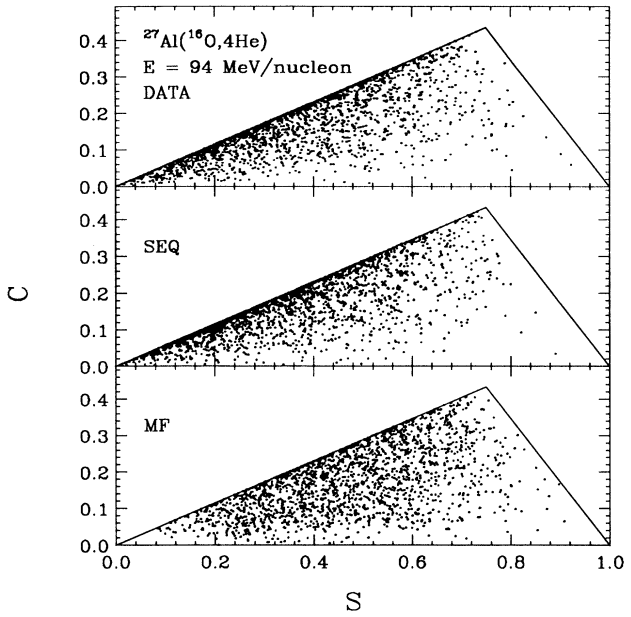

FIG. 20. Comparison between the experimental and the simulated SEQ and MF sphericity-coplanarity distributions for the reaction $^{16}O+^{27}Al \rightarrow 4He$ at 94 MeV/nucleon.

is observable.

Similar results can be obtained directly from the analysis of the eigenvalues of the kinetic tensor instead of that of coplanarity and sphericity. Working with the reduced eigenvalues λ_1', λ_2', and λ_3', normalized to $\lambda_1'+\lambda_2'+\lambda_3'=1$, it is possible to perform an alternative representation of the event shape in momentum space by a kind of Dalitz triangle as in Fig. 21. In this figure λ_3', λ_2', and λ_1' represent the distances of each point from the left, right, and bottom side of the triangle. The special points P, D, and S are relative to pencil-like ($\lambda_1'=1$, $\lambda_2'=\lambda_3'=0$), disklike ($\lambda_1'=\lambda_2'=\frac{1}{2}$, $\lambda_3'=0$), and spherical ($\lambda_1'=\lambda_2'=\lambda_3'=\frac{1}{3}$) events, respectively. As one can see, also in this case the experimental distribution is closer to a sequential-emission picture than to a multifragmentation one.

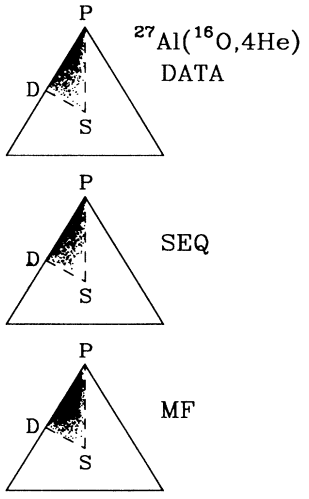

FIG. 21. Dalitz plots for the reduced eigenvalues of the kinetic tensor relative to the experimental and SEQ/MF simulated data for the reaction $^{16}O+^{27}Al \rightarrow 4He$ at 94 MeV/nucleon.

B. Relative angle distributions

With the aim of identifying observables that may help to elucidate the reaction dynamics, recently Lopez and Randrup [28] examined the kinematical differences between sequential binary fission and multifragmentation and considered a number of observables which could be useful as discriminators between these different disassembly mechanisms. Among these observables, the relative angle between all the breakup fragments in their rest frame has attracted some attention in the last years [31,34,35]. In sequential emission via binary fission, the time steps between emissions are supposed so long that the fragments do not suffer any mutual interaction and the relative angle distribution is governed only by the momentum conservation principle. In the multifragmentation framework, however, the repulsive Coulomb interactions between the fragments modify the relative angle distribution, which tends to suppress the small values and enhance the intermediate ones and produces a subsequent narrowing of the distribution.

At low bombarding energies [31,34,35], the relative angle distribution study has been used to conclude that a sequential projectile breakup process occurs. Figure 22 shows the comparison of the experimental relative angle distribution for the system $^{16}O+^{197}Au$ at 32.5 MeV/nucleon [54] with those generated by our SEQ and MF Monte Carlo simulations. In Fig. 23 the experimental, SEQ, and MF relative angle distributions for the system $^{16}O+^{27}Al$ at 94 MeV/nucleon are reported. The data are well reproduced, even at this incident energy, by sequential emission, in agreement with what has been seen in the previous subsection.

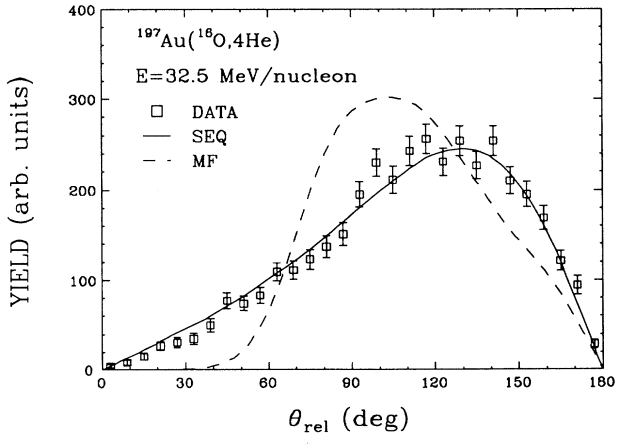

FIG. 22. Relative angle distribution for the reaction ^{197}Au(^{16}O,4He) at 32.5 MeV/nucleon. The experimental data come from Ref. [31]. The solid and dashed curves indicate the results of SEQ and MF simulations described in the text, respectively.

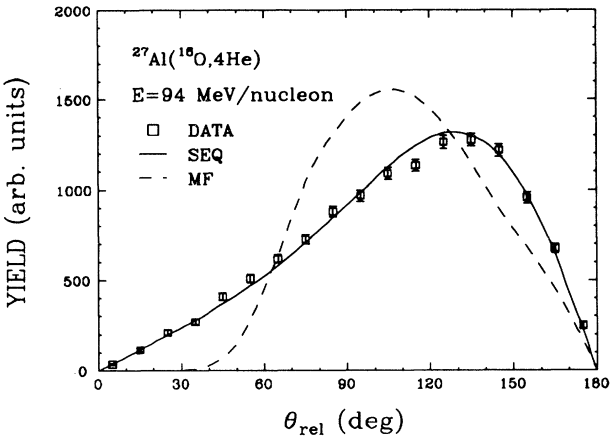

FIG. 23. Relative angle distribution for the reaction ^{27}Al(^{16}O,4He) at 94 MeV/nucleon. The solid and dashed curves indicate the results of SEQ and MF simulations described in the text, respectively.

C. Total coplanarity

The information contained in the global variable analysis conducted so far is only qualitative. Moreover, since the eigenvalues of the velocity tensor and the relative angles among the emitted fragments are evaluated in the reference frame of the disintegrating projectile, all distributions are practically independent of the presence of the target and it is possible to exploit only the effects of the Coulomb interaction on the trajectories of relative motion of the reaction products. More quantitative estimates of the time scale involved in the projectile breakup process can be extracted from the study of the target proximity effect on the decay which allows us to investigate distortions in the distributions of the breakup products that can be attributed to the target Coulomb field. This approach has been already used in the investigations on fissionlike reactions [65], where the deviations of the separation velocity between the fission fragments have been interpreted as due to the proximity of a third fragment during the fission decay and, very recently, on projectile breakup via the 4-He channel [35,55]. Prompt decays might be expected to occur in the immediate vicinity of the target, and the emission angles of the He ions could be also affected by the long-range Coulomb field of the target. Within this context it is rather natural to use the slow radial dependence of the electrical forces to probe the characteristic distances at which the decay actually occurs. In Refs. [66,67] it was shown how one can exploit this feature to identify, via event simulation, appropriate variables that can be used to reveal the nearby presence of the target in order to learn about the time delay involved in the projectile breakup. The analysis method consists of the study of the velocity distribution distortions of the charged particles in the reaction center-of-mass system of reference. In order to characterize quantitatively the distortions in the velocity distributions, we used the total coplanarity C_T calculated from the eigenvalues of the normalized velocity tensor

$$V_{ij}=\frac{1}{4N}\sum_{\nu=1}^{4N}(v_i^{(\nu)}-\bar{v}_i)(v_j^{(\nu)}-\bar{v}_j)\ , \tag{6}$$

where

$$\bar{v}_i=\frac{1}{4N}\sum_{\nu=1}^{4N}v_i^{(\nu)} \tag{7}$$

and N is the total number of experimental events. The total coplanarity previously defined qualifies the total velocity distribution of all detected alpha particles and thus differs from values extracted event by event. The reaction plane is not identified in our experiment, and consequently, the velocity tensor has the beam direction as a symmetry axis. Under these particular circumstances the coplanarity of the total distribution can also be written in terms of the variances of the velocity in the beam direction $\sigma_\parallel$ and in a transverse direction $\sigma_\perp$ as follows:

$$C_T=\frac{\sqrt{3}}{4}\left[\frac{1-2(\sigma_\parallel/\sigma_\perp)^2}{1+(\sigma_\parallel/\sigma_\perp)^2}\right]\ . \tag{8}$$

The total coplanarity displays a smooth, monotonic behavior, as a function of the time delay τ involved in the projectile breakup process [66,67], which lends itself to a calibration of the time scale. It is worthwhile emphasizing that the precision of the value of the total coplanarity is much higher than that of the coplanarity calculated event by event since we have here one event with $4N$ particles instead of N events with only four particles (see Ref. [63]).

A series of velocity distributions as a function of the lifetime τ was thus constructed by means of a computer simulation of the reaction, and for each of them, the corresponding value of C_T was derived. In order to do that, we used a semiclassical heavy-ion reaction code [68] which numerically solves the equations of motion to generate the initial conditions of a highly excited projectile whose sequential disintegration follows. The procedure yields relative positions and momenta of the ions at the instant in which the first splitting is set to occur. The origin to measure times, $t=0$, is set at the distance of closest approach. Although several decay chains can be contemplated, we considered only the chain

$$^{16}\mathrm{O}\rightarrow{}^{12}\mathrm{C}+\alpha\rightarrow{}^{8}\mathrm{Be}+\alpha+\alpha\rightarrow 4\alpha\ ,$$

which is the most likely to occur from simple Q-value considerations. At each step of the decay chain, the two fragments are released with random orientations and the excitation energy is recalculated taking into account the Q value for the specified mass partition, the Coulomb interaction energy, and the released kinetic energy. Positions and velocities of all particles are generated in such a way as to conserve linear momentum and to preserve the position of the total center of mass. In agreement with the previous analysis, the decay has been supposed sequential and no effect due to the intrinsic angular momentum of the source has been taken into account.

The results of the calculations are shown for the sake of completeness in Fig. 24, which was already published [56]. All the points of the simulation fall in the shaded area. In contrast to Refs. [66,67], we have here a region

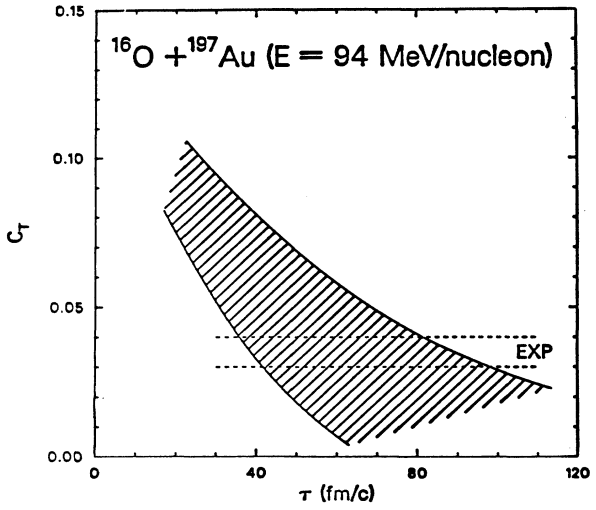

FIG. 24. Total coplanarity C_T vs time delay τ involved in the projectile breakup $^{16}O \rightarrow 4He$ in the reaction $^{16}O + ^{197}Au$ at 94 MeV/nucleon. The shaded area corresponds to the simulated events, while the dashed lines mark the experimental value.

in the (C_T, τ) plane and not a line because we have also taken into account the experimental angular distribution of the projectilelike nucleus. The dashed lines in the figure represent the value of $C_T = 0.035 \pm 0.005$ extracted from the experiment. The error bar takes into account the statistical error due to the finite number of events and the indetermination in the velocity values due to the experimental uncertainties. The results of the analysis are consistent with a time delay of the disassembly process on the order of $\tau = 40-80$ fm/c. This value has been obtained by imposing the previously mentioned conditions on the detection angle ($\theta \leq 20°$) and particle velocity ($v > 8$ cm/ns). Varying these conditions in the same way as in Sec. III A, the corresponding variation of the mean time delay is contained within a factor 1.5. These values are, in any case, several times smaller than those found in Ref. [35] for the reaction ^{159}Tb(^{16}O,4He) at 25 MeV/nucleon and those extracted in Ref. [69] for the system $^{18}O + ^{nat}Ag$ at 84 MeV/nucleon by means of the intensity interferometry technique applied to pairs of identical charged particles.

A so short time scale for the breakup process could provide an explanation of the apparent conflict between the saturation of the PLN excitation energy and the observation of a sequential decay mechanism for the projectile disassembly (i.e., the absence of the opening of a multifragmentation channel). Probably, the projectile breaks sequentially so rapidly that it has no time to gain a larger excitation energy. The validation of this hypothesis needs, however, the analysis of data taken at lower incident energies.

V. SUMMARY AND CONCLUSIONS

In this paper we studied the 4-He channel of the projectile breakup in ^{16}O-induced reactions on ^{27}Al, ^{58}Ni, and ^{197}Au targets at 94 MeV/nucleon. Charged particles have been detected by means of two large-area multidetectors covering the angular range between 3° and 150°, with a total solid angle of about 2π sr. Particular attention has been devoted to the analysis of the space-time evolution of the reaction and to the investigation on the existence of a limit for the excitation energy that a nucleus can sustain before its breaking.

The comparison of the extracted mean values of the projectilelike excitation energy (E^*_{PLN}) with those taken at different lower bombarding energies confirms the previously supposed saturation of the primary projectilelike nucleus excitation energy around 3 MeV/nucleon. This value is found to be independent of the target over a wide range of nuclear masses, indicating that the observed saturation has to be related mainly to the internal structure of the projectile.

The energy sharing between projectile and target has been studied. The value of $R = E^*_{avl}/E^*_{PLN}$ found for the system $^{16}O + ^{197}Au$ is in agreement with those extracted at lower incident energies and leads to the conclusion that energy sharing is very fast and very far from a thermally equilibrated system picture.

In order to get some information about projectile angular momentum and target proximity effects, the spatial distribution of the breakup fragments has been analyzed in the PLN rest frame. No angular momentum effect is visible at 94 MeV/nucleon for any of the targets used in this experiment. On the contrary, effects due to the presence of the target and to the repulsive action of its Coulomb field are clearly observable.

The data have been also submitted to an event-by-event analysis performed in order to extract some global variable distributions describing the fragmenting system and to evaluate the process time scale. The experimental coplanarity-sphericity plots and relative angle distributions have been compared with those calculated through Monte Carlo simulations based on sequential and multifragmentation mechanisms. The data are well reproduced at this incident energy within a sequential-emission picture where no interaction is present among the different fragments.

Finally, a new method consisting of the characterization of the velocity distribution distortions of the emitted fragments by means of the total coplanarity has been used in order to give a quantitative estimate of the time scale of the projectile breakup. The results of the analysis are consistent with a time delay for the disassembly process on the order of $(2-3) \times 10^{-22}$ s.

ACKNOWLEDGMENTS

We wish to thank G. Pollarolo and C. H. Dasso for helpful discussions and for the runs with the code TORINO cited in Ref. [68].

[1] For a review, see, e.g., D. H. Boal, C. K. Gelbke, and B. K. Jennings, Rev. Mod. Phys. **62**, 553 (1990), and references therein.
[2] P. A. De Young, M. S. Gordon, Xiu qin Lu, R. L. McGrath, J. M. Alexander, D. M. de Castro Rizzo, and L. C. Vaz, Phys. Rev. C **39**, 128 (1989).
[3] P. A. De Young *et al.*, Phys. Rev. C **41**, R1885 (1990).
[4] W. G. Gong *et al.*, Phys. Lett. B **246**, 21 (1990).
[5] W. G. Gong *et al.*, Phys. Rev. Lett. **65**, 2114 (1990).
[6] W. G. Gong, W. Bauer, C. K. Gelbke, and S. Pratt, Phys. Rev. C **43**, 781 (1991).
[7] W. G. Gong *et al.*, Phys. Rev. C **43**, 1804 (1991).
[8] W. G. Lynch, L. W. Richardson, M. B. Tsang, R. E. Ellis, C. K. Gelbke, and R. E. Warner, Phys. Lett. **108B**, 274 (1982).
[9] M. B. Tsang *et al.*, Phys. Lett. **148B**, 265 (1984).
[10] M. B. Tsang, C. B. Chitwood, D. J. Fields, C. K. Gelbke, D. R. Klesch, W. G. Lynch, K. Kwiatkowski, and V. E. Viola, Jr., Phys. Rev. Lett. **52**, 1967 (1984).
[11] C. B. Chitwood *et al.*, Phys. Rev. C **34**, 858 (1986).
[12] H. J. Rabe *et al.*, Phys. Lett. B **196**, 439 (1987).
[13] D. Fox, D. A. Cebra, J. Karn, C. Parks, G. D. Westfall, and W. K. Wilson, Phys. Rev. C **36**, 640 (1987).
[14] D. Fox, D. A. Cebra, J. Karn, C. Parks, A. Pradhan, A. Vander Molen, J. Van der Plicht, G. D. Westfall, W. K. Wilson, and R. S. Tickle, Phys. Rev. C **38**, 146 (1988).
[15] C. A. Ogilvie *et al.*, Phys. Lett. B **231**, 35 (1989).
[16] C. A. Ogilvie *et al.*, Phys. Rev. C **40**, 2592 (1989).
[17] D. Ardouin *et al.*, Nucl. Phys. **A514**, 564 (1990).
[18] W. K. Wilson *et al.*, Phys. Rev. C **41**, R1881 (1990).
[19] M. B. Tsang *et al.*, Phys. Rev. C **42**, R15 (1990).
[20] P. L. Gonthier, P. Harper, B. Bouma, R. Ramaker, D. A. Cebra, M. Koenig, D. Fox, and G. D. Westfall, Rev. C **41**, 2635 (1990).
[21] W. K. Wilson, R. Lacey, C. A. Ogilvie, and G. D. Westfall, Phys. Rev. C **45**, 738 (1992).
[22] A. Badalà, R. Barbera, A. Palmeri, G. S. Pappalardo, F. Riggi, Bizard, D. Durand, and J. L. Laville, Phys. Rev. C **45**, 1730 (1992).
[23] T. Ethvignot *et al.*, Phys. Rev. C **46**, 637 (1992).
[24] J. Cugnon, J. Knoll, C. Riedel, and Y. Yariv, Phys. Lett. **109B**, 167 (1982).
[25] M. Gyulassy, K. A. Frankel, and H. Stöcker, Phys. Lett. **110B**, 185 (1982).
[26] P. Danielewicz and M. Gyulassy, Phys. Lett. **129B**, 283 (1983).
[27] J. Cugnon and D. L'Hote, Nucl. Phys. **A397**, 519 (1983).
[28] J. A. Lopez and J. Randrup, Nucl. Phys. **A491**, 477 (1989).
[29] C. A. Ogilvie, D. A. Cebra, J. Clayton, S. Howden, J. Karn, A. Vander Molen, G. D. Westfall, W. K. Wilson, and J. S. Winfield, Phys. Rev. C **40**, 654 (1990).
[30] J. Peter *et al.*, Nucl. Phys. **A519**, 611 (1990).
[31] B. A. Harmon, J. Pouliot, J. A. Lopez, J. Suro, R. Knop, Y. Chan, E. Di Gregorio, and R. G. Stokstad, Phys. Lett. B **235**, 234 (1990).
[32] D. A. Cebra, S. Howden, J. Karn, A. Nadasen, C. A. Ogilvie, A. Vander Molen, G. D. Westfall, W. K. Wilson, J. S. Winfield, and E. Norbeck, Phys. Rev. Lett. **64**, 2246 (1990).
[33] H. W. Barz, D. A. Cebra, H. Schulz, and G. D. Westfall, Phys. Lett. B **267**, 317 (1991).
[34] J. Suro, Y. D. Chan, J. A. Scarpaci, R. G. Stokstad, K. Möhring, and T. C. Schmidt, Nucl. Phys. **A548**, 353 (1992).
[35] R. J. Charity *et al.*, Phys. Rev. C **46**, 1951 (1992).
[36] K. G. R. Doss *et al.*, Phys. Rev. Lett. **59**, 2720 (1987).
[37] H. H. Gutbrod, K. H. Kampert, B. W. Kolb, A. M. Poskanzer, H. G. Ritter, and H. R. Schmidt, Phys. Lett. B **216**, 267 (1989).
[38] D. Krofcheck *et al.*, Phys. Rev. Lett. **63**, 2028 (1989).
[39] C. A. Ogilvie *et al.*, Phys. Rev. C **42**, R10 (1990).
[40] J. P. Sullivan *et al.*, Phys. Lett. B **249**, 8 (1990).
[41] D. Krofcheck *et al.*, Phys. Rev. C **43**, 350 (1991).
[42] J. Jiang *et al.*, Phys. Rev. Lett. **68**, 2739 (1992).
[43] E. Suraud, Nucl. Phys. **A462**, 109 (1987), and references therein.
[44] J. C. Steckmeyer *et al.*, Nucl. Phys. **A500**, 372 (1989).
[45] D. X. Jiang *et al.*, Nucl. Phys. **A503**, 560 (1989).
[46] D. Jacquet *et al.*, Nucl. Phys. **A511**, 195 (1990).
[47] M. Morjean *et al.*, Nucl. Phys. **A524**, 179 (1991).
[48] E. Crema *et al.*, Phys. Lett. B **258**, 266 (1991).
[49] E. Piasecki *et al.*, Phys. Rev. Lett. **66**, 1291 (1991).
[50] J. Pouliot *et al.*, Phys. Lett. B **223**, 16 (1989).
[51] R. Wada *et al.*, Phys. Rev. C **39**, 497 (1989).
[52] K. A. Griffioen, B. J. Gluckman, R. J. Meijer, P. Decowski, and R. Kamermans, Phys. Rev. C **40**, 1647 (1989).
[53] K. A. Griffioen *et al.*, Phys. Lett. B **237**, 24 (1990).
[54] J. Pouliot, Y. Chan, D. E. Di Gregorio, B. A. Harmon, R. Knop, C. Moisan, R. Roy, and R. G. Stokstad, Phys. Rev. C **43**, 735 (1991).
[55] J. Pouliot, *et al.*, Phys. Lett. B **263**, 18 (1991).
[56] A. Badalà, R. Barbera, A. Palmeri, G. S. Pappalardo, F. Riggi, G. Pollarolo, and C. H. Dasso, Phys. Lett. B **299**, 11 (1993).
[57] K. Möhring, T. Srokowski, D. H. E. Gross, and H. Homeyer, Phys. Lett. B **203**, 210 (1988).
[58] K. Möhring, T. Srokowski, and D. H. E. Gross, Nucl. Phys. **A533**, 333 (1991).
[59] G. Bizard, A. Drouet, F. Lefebvres, J. P. Patry, B. Tamain, F. Guilbault, and C. Lebrun, Nucl. Instrum. Methods A **244**, 483 (1986).
[60] A. Peghaire *et al.*, Nucl. Instrum. Methods A **295**, 365 (1990).
[61] R. Barbera *et al.*, Nucl. Phys. **A518**, 767 (1990).
[62] R. Hagedorn, *Relativistic Kinematics* (Benjamin, New York, 1963).
[63] J. P. Bondorf, C. H. Dasso, R. Donangelo, and G. Pollarolo, Phys. Lett. B **240**, 28 (1990).
[64] E. Byckling and K. Kajantie, Nucl. Phys. **B9**, 568 (1969).
[65] P. Glässel, D. v. Harrach, H. J. Specht, and L. Grodzins, Z. Phys. A **310**, 189 (1983).
[66] J. P. Bondorf, C. H. Dasso, G. Massari, and G. Pollarolo, in *Proceedings of the XXIX International Winter Meeting on Nuclear Physics,* Bormio, Italy, 1991, edited by I. Iori (Ricerca Scientifica ed Educazione Permanente, Milano, 1991).
[67] J. P. Bondorf, C. H. Dasso, G. Massari, and G. Pollarolo, Phys. Rev. C **46**, 374 (1992).
[68] C. H. Dasso and G. Pollarolo, Comput. Phys. Commun. **50**, 341 (1988).
[69] R. Trockel *et al.*, Phys. Rev. Lett. **59**, 2844 (1987).